

THE SERIAL RESONANT ANTENNA FOR THE LARGE FIELD OF VIEW MAGNETIC RESONANCE IMAGING

Bo Zhu^{1, 2, *}, Ed Xuekui Wu¹, Patrick Peng Gao¹, Peng Cao¹, and Lijun Jiang¹

¹Department of Electrical and Electronic Engineering, The University of Hong Kong, Hong Kong SAR, China

²Department of Electronic Engineering, Nanjing University, China

Abstract—A serial resonant antenna for the large field of view (FOV) magnetic resonance imaging (MRI) is presented. It consists of metallic patches cascaded through lumped capacitors in serial on the top layer of a grounded dielectric substrate. The theoretical analysis show that at the resonant frequency, uniformly distributed current with zero phase delay is produced independent of the antenna length, hence a uniform magnetic field for large FOV MRI can be achieved. Integrated with the L-shaped tunable matching network, the antenna can be tuned easily to operate rigorously at the working frequency of the MRI system. The numerical modeling, physical fabrication and measurement, as well as the phantom imaging are carried out to design, characterize and verify the performance of the proposed antenna for MRI.

1. INTRODUCTION

Magnetic resonance imaging (MRI) is a widely accepted radiology tool to image body tissues [1]. The nuclear spin of the hydrogen proton of human body produces the magnetic dipole moment. In MRI, a strong DC magnetic field is applied to make the magnetic dipole moments process around the direction of the DC magnetic field with the precession frequency proportional to the magnetic field strength. Then, a radio frequency (RF) magnetic field with the frequency equal to that of the precession is applied. It transports energy into protons through resonance. After the RF pulse, the excited protons return to the equilibrium state and emit RF signals. These signals are then

Received 26 November 2012, Accepted 25 January 2013, Scheduled 28 January 2013

* Corresponding author: Bo Zhu (bzhu@nju.edu.cn).

picked up by the RF coil to construct the tissue image based on the fact that the relaxation time of hydrogen protons varies in different tissues.

The MRI system can be categorized according to the strength of the applied DC magnetic field. The major advantages of the high magnetic field MRI system is that it increases the nuclear magnetic resonance sensitivity to offer high resolution images [2–5]. As DC magnetic field is strong such as in the 7 Tesla (T) MRI system, the center frequency of the RF pulse is also increased and the RF wavelength becomes shorter proportionally. When the wavelength is comparable with the RF coil size, which is often the case in the large field of view (FOV) imaging such as the whole body imaging, wave physics become dominant and the electromagnetic (EM) fields generated by each part of the coil interfere with each other constructively and destructively. This leads to the non-uniform EM field and low imaging quality [6]. The high operation frequency in high field MRI also increases the radiation loss, which leads to degraded quality factor and signal to noise ratio [7, 8]. Hence achieving large area of uniform field is a challenging but critical issue for the high field MRI with large FOV.

Conventional volume coils, such as birdcage coils, are made up by the inductor and capacitor network unit cell assembled into a ring. It works quite similar to a ring resonator, and provides uniform magnetic field in the transverse cross section of the coil in its first resonant mode [9]. With the increased operation frequency in the high field MRI, the electrical dimension of birdcage coils becomes bigger and wave phenomenon occurs. The current on the coil radiates EM waves like an antenna leading to lower Q , and the magnetic field produced by the current no longer obeys the Biot-Savart's law resulting in non-uniform distribution. In order to solve this problem, volume coils made up of TEM resonators are invented [10–13]. The TEM resonator comprises multiple coupled transmission line resonators. The uniform magnetic field distribution can be achieved in the transverse cross section in the lowest resonant mode. Since the TEM mode doesn't radiate, the radiation loss of such coil is greatly reduced. A variety of volume coils have been developed from the TEM resonator because of its advantages [6, 7, 14]. However, wave phenomenon still exists along the longitudinal direction of the coil so that it is still difficult to obtain a uniform magnetic field along that direction, especially for the whole body coil.

Metamaterials, which is artificial composite structure with designable constitutive parameters, have been introduced as a lens to focus the RF magnetic field to improve field penetration depth

and SNR in MRI [15,16]. Recently, the composite right/left handed zeroth-order resonant antenna, another kind of metamaterial, has been proposed as the RF coil component to obtain uniform magnetic field distribution in the longitudinal direction [17,18]. This antenna resonates with uniform field distribution and zero phase delay independent of the antenna length at the frequency transition point between the left-handed and right-handed operation regime. In this paper, we presented a different serial resonant antenna with a much simpler configuration for MRI imaging. Integrated with a tunable matching network, theoretically this antenna can be tuned to operate rigorously at 300.3 MHz for 7.05 T MRI system with arbitrary antenna physical length. It offers uniform magnetic field distribution of zero phase delay along the antenna length's direction so as to achieve the large FOV in the MRI imaging.

2. STRUCTURE AND THEORETICAL ANALYSIS

Figure 1(a) shows the configuration of the proposed serial resonant antenna with the tunable impedance matching network. The transmission line part of the antenna is composed of five rectangular metallic patches on the top layer of a grounded dielectric substrate. Capacitors shown in blue are loaded in serial connection with the metallic patches. The transmission line is terminated by a short at one end and connected to a tunable L-shaped matching network at the other end. The serial branch of the matching network consists of a meanderline inductor and a capacitor trimmer in serial connection, and the parallel branch is composed of a lumped capacitor and a capacitor trimmer in parallel connection.

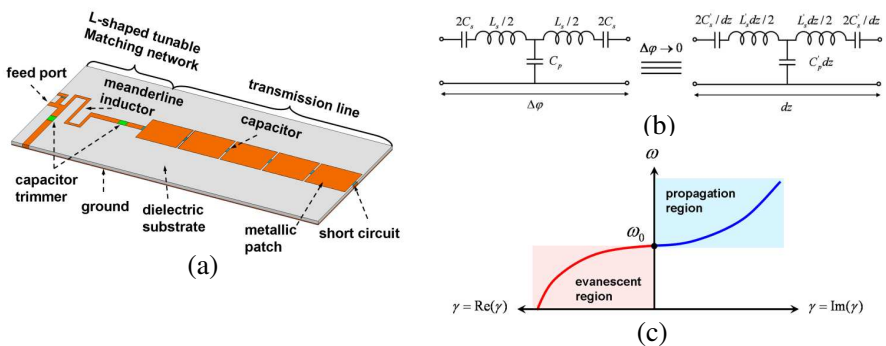


Figure 1. (a) Schematic of the serial resonant antenna. (b) Circuit model for the unit cell. (c) Conceptual propagation constant of the transmission line part.

The metallic patches behave as inductors when the high frequency current flows on them. Hence, the proposed antenna can be modeled as a periodic circuit network with the unit cell shown in Fig. 1(b). The serial branch of the unit cell composed of capacitors in serial connection with inductors represents the lumped capacitors and metallic patches in the antenna, while the parallel branch of the unit cell is composed of a capacitor taking into account the capacitance between the top layer and ground plane of the antenna. Although the unit cell in any physical circuit has a specific length, the phase delay across each unit cell is only related to parametric values of lumped or equivalent lumped elements such as inductors and capacitors in the unit cell rather than the physical length of the unit cell. When the operating frequency is equal to the serial resonant frequency of the inductor L_s and capacitor C_s in the serial branch of the unit cell, the serial impedance of the unit cell is zero such that the phase delay across the unit cell is zero. As a result, the periodic circuit network can be approximated as a uniform transmission line with the distributed circuit parameters obtained by homogenizing the lumped circuit element parameter along the unit cell, as illustrated in Fig. 1(b). Here, $L'_s = L_s/p$, $C'_s = C_s/p$, and $C'_p = C_p/p$ are the inductance and capacitance per unit length of the transmission line, where p is the physical length of the unit cell.

The telegraph equation for the transmission line composed of such unit cell is

$$\frac{dU(z)}{dz} = -ZI(z), \quad (1)$$

$$\frac{dI(z)}{dz} = -YU(z), \quad (2)$$

where $Z = j\omega L'_s + \frac{1}{j\omega C'_s}$ and $Y = j\omega C'_p$, if the energy loss is ignored. Differentiate (1) and (2) with regard to z once more, and insert (1) and (2) into the derived second order differential equations, we will get the decoupled second order ordinary differential equations about $U(z)$ and $I(z)$ respectively. The general solutions of $U(z)$ and $I(z)$ can be written as

$$U(z) = Ae^{-\gamma z} + Be^{\gamma z}, \quad (3)$$

$$I(z) = \frac{1}{Z_0} (Ae^{-\gamma z} - Be^{\gamma z}), \quad (4)$$

where $\gamma = \sqrt{ZY}$ is the propagating constant and $Z_0 = \sqrt{Z/Y}$ is the characteristic impedance. Eqs. (3) and (4) represent waves propagating in opposite directions, similar to the waves in the conventional transmission line. However, since the serial impedance Z is the serial impedance of an inductance and a capacitance, it will be an inductive

impedance when $\omega L'_s > 1/(\omega C'_s)$ such that γ be a purely imaginary number supporting propagating waves. For $\omega L'_s < 1/(\omega C'_s)$, Z is a capacitive impedance, and γ be a real number supporting evanescent wave. Away from the resonant frequency, the propagation constant can be approximated as

$$\begin{aligned}\gamma &= \sqrt{ZY} = j\sqrt{C'_p L'_s (2 \times \omega_0 \times \Delta\omega + \Delta\omega^2)} \\ &\approx j(2 \times \Delta\omega \times C'_p)^{\frac{1}{2}} \left(\frac{L'_s}{C'_s}\right)^{\frac{1}{4}},\end{aligned}\quad (5)$$

where ω_0 is the resonant frequency and $\Delta\omega = \omega - \omega_0$. Fig. 1(c) conceptually illustrates the dependence of γ on frequency ω given L'_s and C'_s . Below the serial resonant frequency $\omega_0 = 1/\sqrt{L'_s C'_s}$, Z is a capacitance so that γ is a real number and waves are attenuated but with zero phase delay along the transmission line. Above the resonant frequency ω_0 , Z is an inductance such that γ is a purely imaginary number supporting propagating waves, similar to conventional transmission line. It can be known from (5) that γ is still close to zero if $\Delta\omega$ is small by properly choosing the parallel as well as serial capacitance and inductance. Hence, both wave attenuation and propagation phase delay on either side of the serial resonance frequency can be ignored in the frequency band around the resonant frequency, which is sufficiently large to include the frequency spectrum component of the RF pulse in MRI that is normally several kilohertz. Since this phenomenon is dependent only on the serial resonant frequency of the unit cell instead of the total length of the transmission line, it is capable of producing uniformly distributed magnetic field along the antenna with arbitrary length theoretically. This feature can be applied in RF coil design for MRI where the uniform RF magnetic field in a large volume is desired.

In order to generate stronger magnetic field, the transmission line is terminated by a short so as to produce stronger uniform current on it. The input impedance of the short-terminated transmission line is calculated as $Z_{in}(s) = Z_0 \tanh(\gamma s)$, where s is the length of the transmission line. It is clear that Z_{in} is equivalent to a capacitor with the operation frequency below the resonant frequency, and an inductor when the operation frequency is a little bit higher than the resonant frequency.

3. FULL WAVE SIMULATION

To fully characterize the serial resonant antenna for MRI, we designed a prototype antenna as depicted in Fig. 1(a) for the 7.05 T MRI

system. Both full wave simulation and experiment study were carried out. Commercial EM solver HFSS is used in the simulation. The permittivity of the substrate is 4.4 with the loss tangent 0.02, and the metal is modeled as copper with the conductivity of 5.8×10^7 S/m. The lumped capacitor C_s in each unit cell is 68 pF. Each rectangular patch of the antenna has the dimension of 26 mm \times 21 mm such that the serial resonance occurs around 300.3 MHz which is the operating frequency of the 7.05 T MRI system. The gap between two adjacent patches is 1 mm. The dielectric substrate is 2 mm thick. A lumped port with 50Ω resistance is assigned to the feed port of the antenna. The transmission line part of the antenna is terminated by a short. The net input power is 1 W in the simulation. The details of the matching network are given in Part 4.

The simulated maximum electric current, magnetic field and electric field at the antenna aperture are demonstrated in Fig. 2 at 300.3 MHz with 1 W net input power. As it can be seen in Fig. 2(a), the current magnitude is uniformly distributed along the antenna without phase delay. This current produces the magnetic field which has uniform strength and zero phase delay along the propagation direction. Fig. 2(b) shows the magnetic field distribution within a region of 30 mm

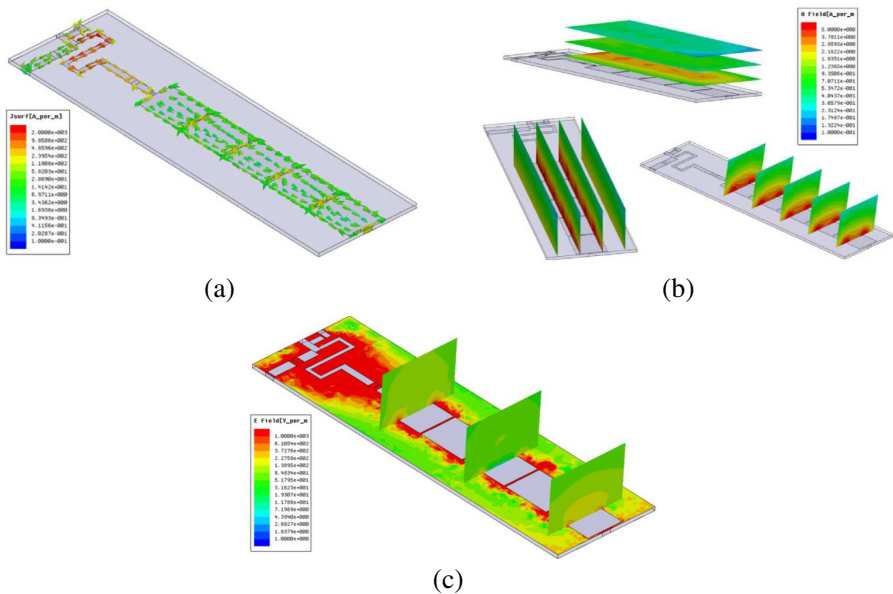


Figure 2. Simulated maximum (a) surface current, (b) magnetic field, and (c) electric field at 300.3 MHz with 1 W net input power.

above the antenna aperture. It can be observed that magnetic field has a constant instantaneous amplitude distribution along the transmission line. The field gets weaker away from the aperture as expected.

Safety issue is important in high field MRI. Fig. 2(c) depicts the maximum electric field distribution at 1 W net input power. Due to the series resonance, high electric potential and strong electric field occur where the total voltage on serial inductors is not equal to that on serial capacitors in the transmission line, as can be seen in the aperture electric field distribution. However, the electric field strength decays fast away from the aperture with only dozens of volts per meter.

We also compared the electric field, voltage and current distributions on different parts of the antenna with their withstanding ratings under 1 W net input power. Since the input impedance of the transmission line is small at resonant frequency, the voltage drops mainly on the matching network where the strong electric field is observed in Fig. 2(c). The current density is also large on the matching network because its conductor is thin. The comparison between the simulated results under 1 W net input power with withstanding ratings of various components of the antenna is listed in Table 1. This information can be referenced for the antenna safety design.

4. FABRICATION AND EXPERIMENT

According to the optimization by simulation, a prototype antenna with the dimension of $6\text{ cm} \times 20\text{ cm} \times 0.2\text{ cm}$ was built for practical experiment

Table 1. Comparison of simulated field, voltage and current (1 W) with withstanding ratings.

Component	Voltage or Electric Field Intensity (simulation/rating)	Current (simulation /rating)
Trimmer	50 V/2000 V	N/A
Capacitor	10 V/500 V	N/A
Gap btw. patches	10 V/1000 V	N/A
Matching network	30 V/mm/1000 V/mm	2 A/2 A
Short termination	N/A	2 A/4.5 A
Max. E field in Substrate	30 V/mm/1000 V/mm	N/A
SMA, coaxial cable, SMA/BNC adaptor	7 V/N/A	0.14 A/N/A

and medical imaging test. FR4 dielectric board with permittivity of 4.4 and loss tangent of 0.02 is used as the substrate. The bottom layer of the board is a full metallic ground, and copper paste is cut and adhered to the top layer of the board as the rectangular metallic patch. The lumped capacitor connecting the adjacent patches is non-magnetic with the model number of ATC100B680JWN500X.

The center frequency of the RF pulse in MRI system is usually fixed. However, many factors, such as fabrication tolerance, coupling between the antenna and imaged object as well as other parts of the MRI system, etc., may affect the operation of the RF antenna and lead to the deviation of resonance frequency and bandwidth from the designed ones. Therefore we integrated a tunable L-shaped matching network into the antenna so that its input impedance can be transformed to $50\ \Omega$ at 300.3 MHz precisely in order to improve SNR in imaging, as shown in Fig. 1(a). It consists of tunable impedances in both parallel and serial branches respectively. Since the real part of the input impedance of the transmission line part is smaller than $50\ \Omega$ around 300 MHz according to the simulation results, the parallel branch is placed closer to feed source and serial branch placed closer to the transmission line part [19]. Since the imaginary part of input impedance of the short-terminated transmission line can be either capacitive or inductive around serial resonant frequency, corresponding inductance and capacitance are needed in the matching network for the reactive energy compensation. Hence, the serial branch of the matching network is composed of a meanderline inductor in series connection with a capacitor trimmer so that both effective capacitance and effective inductance can be achieved by tuning the trimmer's capacitance. The parallel branch consists of a lumped capacitor and a capacitor trimmer in parallel connection to provide necessary capacitance tuning range. Both the lumped capacitor and the capacitor trimmer are non-magnetic. The two trimmers' model numbers are NMAJ40HVE and NMAP40HV respectively. The parasitic inductance of the capacitor trimmer should be considered at 300.3 MHz due to its relatively large size (14.22 mm in length and 7.62 mm in diameter). Measurement results show that the parasitic inductance is about 8 nH and 11 nH for the two trimmers respectively. In our design, extra serial capacitors are used to compensate the parasitic inductance of the trimmer at 300.3 MHz. Fig. 3 shows the unloaded S_{11} of the fabricated prototype antenna measured with Agilent 8753ES vector network analyzer. After tuning the two capacitor trimmer conveniently, the input impedance is matched to $50\ \Omega$ at 300.3 MHz exactly. The unloaded Q factor is calculated to be 110.5 by the formula $2 \times f/\Delta f$, where f is the impedance match

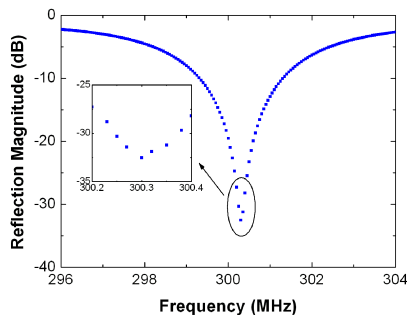


Figure 3. Measured S_{11} of the fabricated prototype antenna. Inset shows the enlarge S_{11} around 300.3 MHz.

frequency and Δf is the -3 dB bandwidth in reflection [20]. When a palm is put about $1 \sim 2$ centimeter above the antenna aperture, the Q factor drops to 106.1 with roughly 0.2 MHz center frequency downward shift. The relatively small difference between the loaded and unloaded Q factor could be attributed to the fast attenuation of the magnetic near field that is proportional to squared distance from the aperture because of the image current produced by the ground plane.

To validate the FOV property of the proposed antenna, phantom imaging test is carried out in a 7.05 T MRI system. The CuSO_4 phantom used in the experiment is cylindrical shaped with one tapered end and one round end. Its length is 12 cm, diameter 25 mm, and concentration 5 g/l. It is tied over the antenna aperture using tapes, and put into the MRI system with the antenna aperture downward. Sponge is inserted between the antenna aperture and phantom near its round end in order to adjust the horizontal position of the phantom. Fig. 4 exhibits the acquired image in the transverse cross section and longitudinal cross section parallel with the antenna aperture. The sequence used was 2D FLASH, FA = 30 deg, TE = 5 ms, TR = 200 ms, FOV = $60 \times 60 \text{ mm}^2$, Matrix = 128×128 . Since the antenna is over the phantom inside the MRI system, the image brightness is not uniform as can be observed in the transverse cross section image shown in Fig. 4(a). The upper brighter region is closer to the antenna aperture. However, it is observed in Fig. 4(b) that the brightness along the longitudinal direction of the antenna is uniform, indicating that the magnetic field produced by the proposed antenna is uniform and can provide large FOV MRI imaging. The SNR of Fig. 4(a) is calculated as 62.4 and that of Fig. 4(b) 70.95 using the sample points denoted by blue signs. The irregular shadow region at the bottom of Fig. 4(b) is

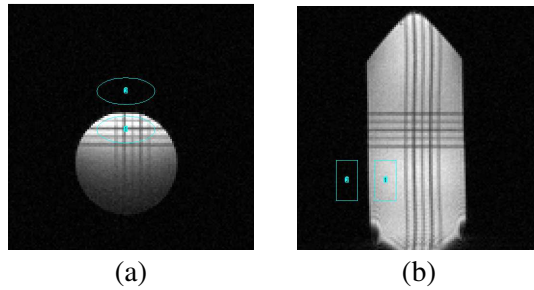


Figure 4. Phantom image in (a) transverse plane and (b) longitudinal plane parallel with the antenna aperture.

caused by the sponge. The dark lines in the image indicate the center of DC magnetic field of the system for positioning the object.

5. CONCLUSION

We have presented the serial resonant antenna with a simple structure for the large FOV MRI imaging. Theoretical analysis shows that the uniform field distribution without propagation phase delay occurs at serial resonance frequency which is independent of the antenna length. Theoretically this feature allows generating uniform field in arbitrary length. Based on this fact, we designed such an antenna with the tunable impedance matching network. Experiment and simulation results show that this antenna can be easily tuned to operate rigorously at MRI system frequency with uniform magnetic field in a large area. It is further successfully applied to image the phantom in a MRI system. Furthermore, in order to obtain large FOV in a volume, a cylindrical coil can be built by arranging the proposed antenna as the unit cell on the edge of a cylinder evenly.

ACKNOWLEDGMENT

We thank Dr. Shulabh Gupta for his kind help in antenna Q factor measurement. This work was supported by the HKU Small Project Funding (201007176196).

REFERENCES

1. Jin, J., *Electromagnetic Analysis and Design in Magnetic Resonance Imaging*, CRC Press, 1988.

2. Chen, C. N., V. J. Sank, S. M. Cohen, and D. I. Hoult, "The field dependence of NMR imaging. I. Laboratory assessment of signal-to-noise ratio and power deposition," *Magn. Reson. Med.*, Vol. 3, No. 5, 722–729, 1986.
3. Robitaille, P. M., A. M. Abduljalil, A. Kangarlu, X. Zhang, Y. Yu, R. Burgess, S. Bair, P. Noa, L. Yang, H. Zhu, B. Palmer, Z. Jiang, D. M. Chakeres, and D. Spigos, "Human magnetic resonance imaging at 8 T," *NMR Biomed.*, Vol. 11, No. 6, 263–265, 1998.
4. Ugurbil, K., M. Garwood, J. Ellermann, K. Hendrich, R. Hinke, X. Hu, S. G. Kim, R. Menon, H. Merkle, and S. Ogawa, "Imaging at high magnetic fields: Initial experiences at 4 T," *Magn. Reson. Q.*, Vol. 9, No. 4, 259–277, 1993.
5. Ugurbil, K., X. Hu, W. Chen, X. H. Zhu, S. G. Kim, and A. Georgopoulos, "Functional mapping in the human brain using high magnetic fields," *Philos. Trans. R. Soc. Lond. B Biol. Sci.*, Vol. 354, No. 1387, 1195–213, 1999.
6. Pang, Y., Z. Xie, D. Xu, D. A. Kelley, S. J. Nelson, D. B. Vigneron, and X. Zhang, "A dual-tuned quadrature volume coil with mixed $\lambda/2$ and $\lambda/4$ microstrip resonators for multinuclear MRSI at 7 T," *Magn. Reson. Imaging*, Vol. 30, 290–298, 2012.
7. Zhang, X., K. Ugurbil, R. Sainati, and W. Chen, "An inverted-microstrip resonator for human head proton MR imaging at 7 Tesla," *IEEE Trans Biomed Eng.*, Vol. 52, No. 3, 495–504, 2005.
8. Vaughan, J. T., M. Garwood, C. M. Collins, W. Liu, L. DelaBarre, G. Adriany, P. Andersen, H. Merkle, R. Goebel, M. B. Smith, and K. Ugurbil, "7 T vs. 4 T: RF power, homogeneity, and signal-to-noise comparison in head images," *Magn. Reson. Med.*, Vol. 46, No. 1, 24–30, 2001.
9. Hayes, C. E., W. A. Edelstein, J. F. Schenck, O. M. Mueller, and M. Eash, "An efficient, highly homogeneous radiofrequency coil for whole-body NMR imaging at 1.5 T," *J. Magn. Resonance*, Vol. 63, 622–628, 1985.
10. Röschmann, P., "High-frequency coil system for a magnetic resonance imaging apparatus," U.S. Patent 4 746 866, May 24, 1988.
11. Bridges, J. F., "Cavity resonator with improved magnetic field uniformity for high frequency operation and reduced dielectric heating in NMR imaging devices," U.S. Patent 4 751 464, Jun. 14, 1988.
12. Vaughan, J. T., H. P. Hetherington, J. O. Otu, J. W. Pan, and G. M. Pohost, "High frequency volume coils for clinical NMR imaging and spectroscopy," *Magn. Reson. Med.*, Vol. 32, 206–218, 1994.

13. Röschmann, P., “Radiofrequency penetration and absorption in the human body: Limitations to high-field whole-body nuclear magnetic resonance imaging,” *Med. Phys.*, Vol. 14, No. 6, 922–932, Nov.–Dec. 1987.
14. Pang, Y., Z. Xie, Y. Li, D. Xu, D. Vigneron, and X. Zhang, “Resonant mode reduction in radiofrequency volume coils for ultrahigh field magnetic resonance imaging,” *Materials*, Vol. 4, 1333–1344, 2011.
15. Xie, Y., J. Jiang, and S. He, “Proposal of cylindrical rolled-up metamaterial lenses for magnetic resonance imaging application and preliminary experimental demonstration,” *Progress In Electromagnetics Research*, Vol. 124, 151–162, 2012.
16. Freire, M. J., L. Jelinek, R. Marques, and M. Lapine, “On the application of $\mu_r = -1$ metamaterial lenses for magnetic resonance imaging,” *J. Magn. Reson.*, Vol. 203, 81–90, 2010.
17. Rennings, A., J. Mosig, A. Bahr, C. Caloz, M. E. Ladd, and D. Erni, “A CRLH metamaterial based RF coil element for magnetic resonance imaging at 7 Tesla,” *Proc. 3rd European Conference on Antennas and Propagation (EuCAP)*, 3231–3234, Berlin, Germany, Mar. 2009.
18. Rennings, A., P. Schneider, C. Caloz, and S. Orzada, “Preliminary experiments on a CRLH metamaterial zeroth-order resonant coil (ZORC) element for 7 Tesla MRI applications with large field of view,” *Proc. 3rd International Congress on Advanced Electromagnetic Materials in Microwaves and Optics*, 128–136, London, British, Sep. 2009.
19. Pozar, D. M., *Microwave Engineering*, 3rd Edition, John Wiley and Sons Inc., New York, 2005.
20. Mispelter, J., M. Lupu, and A. Briguet, *NMR Probeheads for Biophysical and Biomedical Experiments: Theoretical Principles and Practical Guidelines*, Imperial College Press, London, 2006.